



Stimulation of neural stem cell differentiation by circularly polarized light transduced by chiral nanoassemblies

Aihua Qu^{1,2,5}, Maozhong Sun^{1,2,5}, Ji-Young Kim³, Liguang Xu^{1,2}, Changlong Hao^{1,2}, Wei Ma^{1,2}, Xiaoling Wu^{1,2}, Xiaogang Liu⁴, Hua Kuang^{1,2}✉, Nicholas A. Kotov³✉ and Chuanlai Xu^{1,2}✉

The biological effects of circularly polarized light on living cells are considered to be negligibly weak. Here, we show that the differentiation of neural stem cells into neurons can be accelerated by circularly polarized photons when DNA-bridged chiral assemblies of gold nanoparticles are entangled with the cells' cytoskeletal fibres. By using cell-culture experiments and plasmonic-force calculations, we demonstrate that the nanoparticle assemblies exert a circularly-polarized-light-dependent force on the cytoskeleton, and that the light-induced periodic mechanical deformation of actin nanofibres with a frequency of 50 Hz stimulates the differentiation of neural stem cells into the neuronal phenotype. When implanted in the hippocampus of a mouse model of Alzheimer's disease, neural stem cells illuminated following a polarity-optimized protocol reduced the formation of amyloid plaques by more than 70%. Our findings suggest that circularly polarized light can guide cellular development for biomedical use.

Cells and tissues are sensitive to light exposure¹, with the light intensity, wavelength and dose known to determine the biological outcomes of the illumination. Despite the universal importance of chirality in biology, cells are not known to be sensitive to the left and right circular polarization of photons. Except for special circumstances when circularly polarized light (CPL) is used for biomedical imaging² and biosensing^{3–5}, circular polarization is believed to make a minimal difference for cellular response because the total number of photons adsorbed by biomolecules for left and right circular polarization differs by only a fraction of a percent. Confirming these expectations, cellular sensitivity to the circular polarization of incident light has not been observed in previous studies of cells with neuronal⁶ and other lineages⁷. Perhaps for these reasons, the biological effects of chiral photons remain largely unknown.

Chiral inorganic nanoparticles (NPs), and especially their assemblies, strongly interact with CPL due to their high polarizability^{8–13}, which may considerably enhance the biological response to chiral photons. Highly localized heat emission¹⁴, in situ chiral catalysis^{15,16} and plasmon-induced nanoscale deformations^{17,18} open several pathways to induce a strong cellular response to photons of specific circular polarization. The advances in gold NP assemblies bridged by DNA^{19–21}, protein²² and other biocompatible polymers²³, combined with better understanding of the dynamics of chiral plasmonic nanostructures under CPL¹⁷, instil confidence that one can engineer nanoassemblies specifically for this function.

Results

Chiroptically active reconfigurable nanoassemblies. Au NPs coated with D-/L-Cys of three different sizes, functionalized with

single-stranded DNA (ssDNA), were used to assemble branched NP assemblies with one 30-nm NP and one 20-nm NP bridged together (Fig. 1a). The branches with dangling 5-nm NPs can be connected to either 30-nm or 20-nm NPs, forming assemblies denoted as $C_{30}S_5-C_{20}$ and $C_{30}-C_{20}S_5$, respectively (Supplementary Table 1). The geometry and chiroptical activity of the assemblies are determined by the chiral Cys coating of the 30-nm and 20-nm core NPs (Methods). The handedness of Cys used for their functionalization is signified by a subscript, for example, $C_{30(b)}S_5-C_{20(l)}$ or $C_{30(l)}S_5-C_{20(b)}$. These nanoassemblies are capable of reconfiguration inside the cell to entangle with nanofilaments of cytoskeleton because the DNA branches, connecting 5-nm and 30-nm NPs, were chosen to be stem-loop sequences (21 bp) complementary to *Fox3* mRNA expressed during neural stem cells (NSCs) differentiation into neurons (Supplementary Fig. 1). The used $C_{30(b)}S_5-C_{20(l)}$ nanoassemblies in most cases reconfigured in the presence of *Fox3* into $C_{30(b)}-C_{20(l)}S_5$ with 5-nm NPs moving from the vicinity of 30-nm NPs to 20-nm ones. The change in geometry of the nanoassemblies was confirmed by tomographic reconstructions of cryo-transmission electron microscopy (TEM) images (Fig. 1b,c).

Circular dichroism (CD) spectra of $C_{30(b)}S_5-C_{20(l)}$ show a negative peak at 524 nm (-63.5 ± 2.7 mdeg), which becomes positive following hybridization of the branches with *Fox3* (37.4 ± 1.4 mdeg; Fig. 1b). Correspondingly, $C_{30(l)}S_5-C_{20(b)}$ displays a positive CD signal of 61.4 ± 2.6 mdeg that becomes negative upon rearrangement (-37.4 ± 1.7 mdeg; Supplementary Figs. 1 and 2). The reconfiguration of $C_{30(b)}S_5-C_{20(l)}$ and $C_{30(b)}-C_{20(l)}S_5$ caused by the *Fox3* sequence is also accompanied by de-quenching of the 6-carboxy-fluorescein (FAM) fluorophore attached to the anti-*Fox3* strand (Supplementary Fig. 3).

¹Key Laboratory of Synthetic and Biological Colloids, International Joint Research Laboratory for Biointerface and Biodetection, Jiangnan University, Wuxi, Jiangsu, China. ²State Key Laboratory of Food Science and Technology, School of Food Science and Technology, Jiangnan University, Wuxi, Jiangsu, China. ³Department of Chemical Engineering, Biointerface Institute, University of Michigan, Ann Arbor, MI, USA. ⁴Department of Chemistry, Faculty of Science, National University of Singapore, Singapore, Singapore. ⁵These authors contributed equally: Aihua Qu, Maozhong Sun. ✉e-mail: kuangh@jiangnan.edu.cn; kotov@umich.edu; xcl@jiangnan.edu.cn

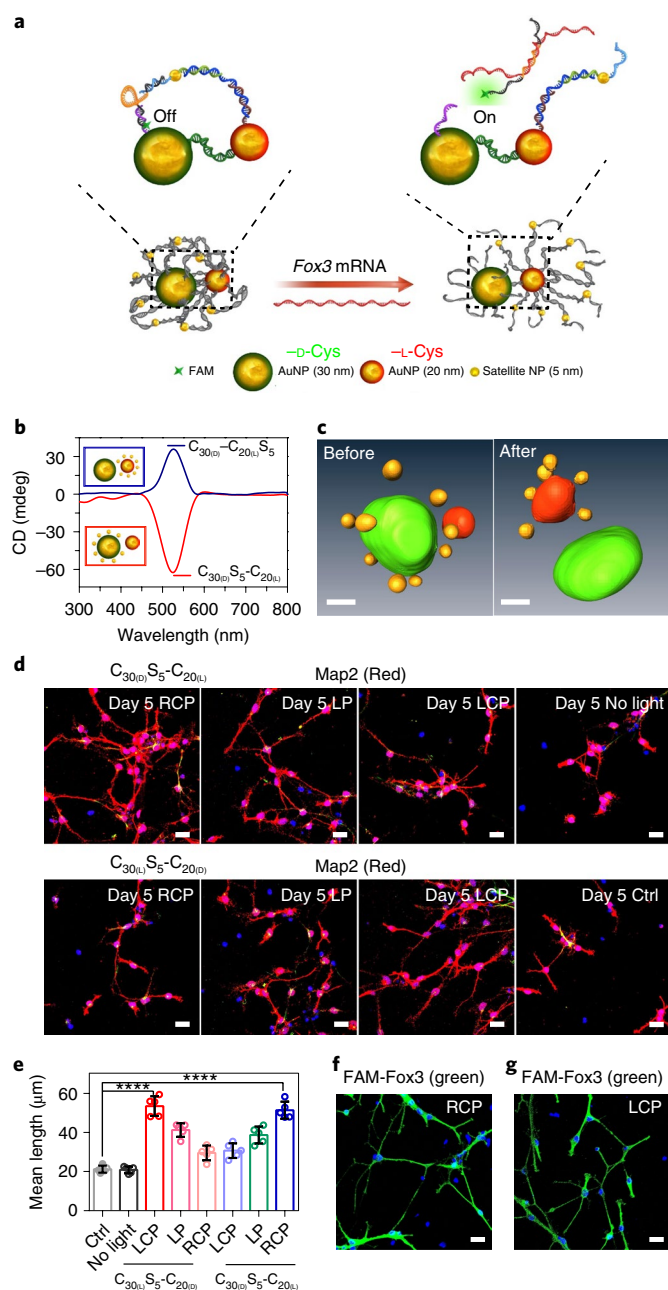


Fig. 1 | CPL accelerates NSCs differentiation. **a**, Schematic of *Fox3* mRNA triggering the configuration transformation of $C_{30(d)}S_5-C_{20(l)}$ nanoassemblies. **b**, CD spectra of $C_{30(d)}S_5-C_{20(l)}$ and $C_{30(d)}-C_{20(l)}S_5$ in phosphate buffered saline (PBS). Insets: schematics of $C_{30(d)}S_5-C_{20(l)}$ (red box) and $C_{30(d)}-C_{20(l)}S_5$ (blue box). **c**, Three-dimensional (3D) tomography of $C_{30(d)}S_5-C_{20(l)}$ before and after transformation. Scale bars, 10 nm. **d**, Confocal images of NSCs incubated with $C_{30(d)}S_5-C_{20(l)}$ (top row) or $C_{30(d)}S_5-C_{20(d)}$ (bottom row) for 4 h each day, and subsequently illuminated with CPL (50 μ J per pulse, 50 Hz, 5 min) for five days, or incubated with $C_{30(d)}S_5-C_{20(l)}$ without illumination for five days; cells without nanoassemblies or light exposure were used as a control. Red, Map2 for mature neurons; blue, 4',6-diamidino-2-phenylindole (DAPI) for nuclei; green, glial fibrillary acidic protein (GFAP) for astrocytes. Scale bars, 20 μ m. RCP, right circularly polarized; LCP, left circularly polarized; LP, linearly polarized. **e**, Neurite mean length of differentiated NSCs. **f,g**, Confocal images of mRNA (*Fox3*) in differentiated NSCs incubated with $C_{30(d)}S_5-C_{20(l)}$ (**f**) or $C_{30(d)}S_5-C_{20(d)}$ (**g**), and illuminated with RCP or LCP light. Scale bars, 20 μ m. **** $P < 0.0001$. Data are presented as mean \pm s.d. ($n = 5$).

The chiroptical activity of the $C_{30(d)}S_5-C_{20(l)}$ and $C_{30(d)}-C_{20(l)}S_5$ nanoassemblies in the visible range primarily arises from the mirror asymmetry of the entire superstructure, with a minor contribution of the local plasmonic enhancement of the biomolecular chirality^{10,13,17,22,24}, which can be concluded from the weak chiroptical activity of the nanoscale components of the assemblies (DNA bridges, individual NPs and their dimers; Supplementary Fig. 2).

To confirm the biological functionality of the $C_{30(d)}S_5-C_{20(l)}$ nanoassemblies, we incubated them with NSC culture for 10 days in the dark. Similar to other plasmonic NPs and their assemblies^{25,26}, $C_{30(d)}S_5-C_{20(l)}$ are transported from the buffer into the cellular cytoplasm. They undergo reconfiguration into $C_{30(d)}-C_{20(l)}S_5$ within the intracellular environment, as confirmed by bio-TEM, confocal microscopy, the temporal progression of CD and photoluminescence spectra (Supplementary Figs. 4–7). The geometrical reorganization of the nanoassemblies can also occur in the dark, triggered by *Fox3* production during the spontaneous differentiation of NSCs.

CPL-accelerated NSC differentiation. In vitro differentiation of NSCs with and without $C_{30}S_5-C_{20}$ was investigated with illumination with 532-nm laser light with variable circular/linear polarizations and on/off illumination patterns. NSCs were illuminated with a 50-Hz pulse rate and energy of 50 μ J per pulse over periods not exceeding 5 min each day for five days. Illumination for 10 min resulted in cell death, presumably from hyperthermia (Supplementary Fig. 8).

We tested the effects of photonic polarization on the neuronal differentiation with right circularly polarized (RCP), left circularly polarized (LCP) and linearly polarized (LP) light. NSCs with $C_{30(d)}S_5-C_{20(l)}$ inside displayed a remarkable increase in neurite length when irradiated with RCP ($51 \pm 4.4 \mu$ m) than in other conditions: dark ($21 \pm 1.7 \mu$ m), LCP ($31 \pm 3.8 \mu$ m) and LP ($39 \pm 4.3 \mu$ m). A similar increase in neurite length ($53 \pm 5.0 \mu$ m) was observed for NSCs with $C_{30(l)}S_5-C_{20(d)}$ under LCP but not for other polarizations (Fig. 1d,e and Supplementary Figs. 8–10). The notable differences in NSC differentiation between these illumination conditions were further confirmed by the activation of FAM luminescence as the *Fox3* mRNA differentiation marker appears (Fig. 1f,g and Supplementary Figs. 11 and 12). Note that hybridization of this mRNA to the nanoassemblies did not appreciably affect expression of the *Fox3*-encoded NeuN protein, a neuron marker²⁷, as established by western blotting and polymerase chain reaction with reverse transcription (RT–PCR) analysis (Fig. 2e,f and Supplementary Figs. 11 and 12).

The chiroplasmonic band in the CD spectra of cells at 524 nm serves as the *Fox3* spectroscopic marker. Its sign and amplitude can also be used to monitor the extent of cell differentiation. The largest change in CD amplitude was, again, for RCP illumination of cells incubated with $C_{30(d)}S_5-C_{20(l)}$ (Fig. 2a) and LCP for cells incubated with $C_{30(l)}S_5-C_{20(d)}$ (Fig. 2b). The CD bands changed not only their magnitude but also their polarity in both cases. Concomitantly, the sign of the CD peaks did not change in any remarkable fashion when NSCs were illuminated with LP or with CPL of opposite handedness than in the previous experiments (Supplementary Figs. 11 and 12). Note that polarity reversal of the CD peak for the $C_{30}S_5-C_{20}$ after reconfiguration does not imply that they are converted into their mirror images¹³ by hybridization with *Fox3*. It only indicates the preferential geometry and the sign of their Osipov–Pickup–Dunmur chirality measure¹⁷.

A flow-cytometric analysis demonstrated that NSCs with $C_{30(d)}S_5-C_{20(l)}$ under RCP displayed ~68-fold greater fluorescence intensity of neurons than astrocytes, which is much higher than for any other conditions, consistent with the CD data (Fig. 2c,d and Supplementary Fig. 11).

Polarity-optimized CPL differentiation of NSCs. The chiroptical polarity of the nanoassemblies changed during the *Fox3*-induced

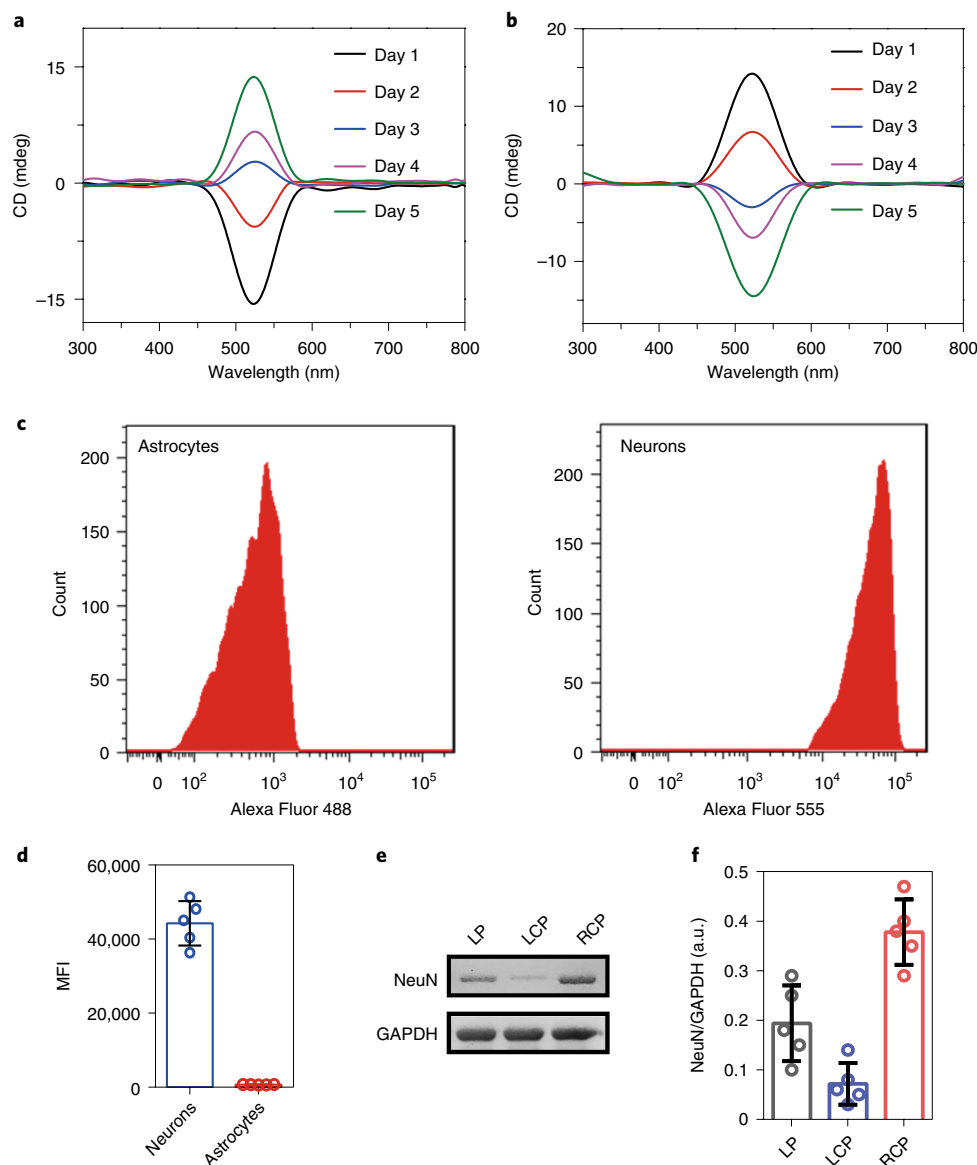


Fig. 2 | Neuron expression of differentiated NSCs under CPL illumination. a,b, CD spectra of differentiated NSCs incubated with C_{30(b)}S₅-C_{20(l)} (**a**) or C_{30(l)}S₅-C_{20(b)} (**b**) and illuminated with RCP or LCP. **c**, Detection of neurons and astrocytes by flow cytometry in differentiated NSCs cultured with C_{30(b)}S₅-C_{20(l)} and illuminated with RCP (Alexa Fluor 488-labelled GFAP; Alexa Fluor 555-labelled Map2). **d**, Mean fluorescence intensity (MFI) for the results in **c**. **e,f**, Western blot for NeuN protein (Fox3 coding) in differentiated neurons incubated with C_{30(b)}S₅-C_{20(l)} and illuminated with CPL; GAPDH (glyceraldehyde-3-phosphate dehydrogenase) acts as a control. A.u., arbitrary units. Original western blot images are provided in Supplementary Fig. 38e,f. Data are presented as mean \pm s.d. ($n = 5$).

reconfiguration from C_{30(b)}S₅-C_{20(l)} into C_{30(b)}-C_{20(l)}S₅. Thus, one may expect that cell differentiation would be further improved by switching the CPL polarity in the course of differentiation, because it will increase the adsorption of photons with the circular polarization corresponding to the current peak polarity in the CD spectrum. To investigate this possibility, three CPL regimens were tested for NSCs with C_{30(b)}S₅-C_{20(l)} in the cytosol, while keeping other illumination conditions and the photothermal energy deposited in the cell culture the same (Supplementary Fig. 13). The CPL polarity each day over the period of five days for the three regimens was as follows: (1) RCP-RCP-RCP-LCP-LCP; (2) RCP-RCP-LCP-LCP-LCP; (3) RCP-RCP-RCP-RCP-LCP (Fig. 3a–c and Supplementary Fig. 14). The highest degree of differentiation, as enumerated by the average length of the neurites, was found for illumination with RCP during the first three days and LCP during the last two days; we will refer

to this as the polarity-optimized CPL illumination protocol (for brevity it will be referred to as RRR-LL) when using C_{30(b)}S₅-C_{20(l)} to accelerate the differentiation of NSCs. The sequence of days with right- and left-handed illumination is consistent with the temporal profile of the conformational changes in C_{30(b)}S₅-C_{20(l)} and the dynamics of its chiroptical activity (Fig. 3d and Supplementary Figs. 14 and 15). Comparing with the mean neurite length of NSC cultures with C_{30(b)}S₅-C_{20(l)} differentiating in the dark ($21 \pm 1.7 \mu\text{m}$), their lengths were $84 \pm 4.1 \mu\text{m}$ and $51 \pm 4.4 \mu\text{m}$ for RRR-LL (Fig. 3c) and RCP-RCP-RCP-RCP-RCP (for brevity referred to as RRRRR) polarity sequences, respectively.

Mirror symmetrically, the polarity-optimized protocol for NSCs incubated with C_{30(l)}S₅-C_{20(b)} was illumination with LCP during the first three days and with RCP for the last two days (LCP-LCP-LCP-RCP-RCP, for brevity LLL-RR). This also resulted

in the highest neurite length increase of $84 \pm 3.5 \mu\text{m}$ (Supplementary Fig. 16) among other polarity protocols for $C_{30(\text{L})}S_5-C_{20(\text{D})}$. It also matched the temporal progression of CD spectra for NSCs with $C_{30(\text{L})}S_5-C_{20(\text{D})}$ (Supplementary Fig. 16).

Analysis for β III-tubulin²⁷, confirmed the accelerated differentiation when NSCs with $C_{30(\text{D})}S_5-C_{20(\text{L})}$ or $C_{30(\text{L})}S_5-C_{20(\text{D})}$ were illuminated by RRR-LL or LLL-RR, respectively (Supplementary Fig. 17), as verified by surface-enhanced Raman spectroscopy (SERS), RT-PCR, fluorescence from FAM-labelled anti-*Fox3* and western blot data for NeuN protein (Supplementary Figs. 16 and 18). Although NSCs were incubated with $C_{30(\text{D})}S_5-C_{20(\text{L})}$ or $C_{30(\text{L})}S_5-C_{20(\text{D})}$ without anti-*Fox3* sequences, the CD intensity did not change during differentiation (Supplementary Figs. 19–23). When nanoassemblies were not present and NSCs were incubated with Cys-modified single NPs or dimers, these cells showed limited neuronal differentiation (Supplementary Fig. 24).

Additional measures of the strong effect of polarity-optimized CPL sequence on neuronal differentiation were (1) the proportions of neurons after differentiation and (2) the degree of Map2 expression. The fluorescence intensity for neurons exceeded that for astrocytes by nearly 100-fold (Fig. 3e,f). The content of Map2 protein was $2.77 \pm 0.31 \text{ ng ml}^{-1}$ in NSCs, which was notably greater than in the cells illuminated with unchanged CPL throughout the five-day cycle ($1.66 \pm 0.18 \text{ ng ml}^{-1}$), and the content in cells without illumination (only $0.72 \pm 0.08 \text{ ng ml}^{-1}$) (Supplementary Fig. 18). Analysis of the early-stage oligodendrocyte marker²⁸ O4 revealed that CPL did not substantially affect the proportion of oligodendrocytes²⁹, which was 25% or 23% with or without CPL illumination, respectively (Supplementary Fig. 25).

The NSCs whose differentiation was accelerated by the polarity-optimized CPL illumination protocol displayed the biological functionality of neurons. We observed fast calcium ion channel activity (Fig. 3g,h), visualized by confocal microscopic images and potassium channel activity recorded by a patch-clamp (Fig. 3i). By contrast, no characteristic currents were observed after illumination in the absence of the nanoassemblies following the RRR-LL protocol (Fig. 3j).

Mechanism of CPL-accelerated NSC differentiation. Considering the potential mechanisms of accelerated differentiation by CPL illumination, we investigated the possibility of thermal activation of neurons, but the difference in deposited thermal energy cannot explain the observed biological response (Supplementary Fig. 13), because no temperature changes were observed (Supplementary Fig. 13). The mechanisms involving local plasmonic catalysis of some specific biomolecules also contradicted multiple benchmark experiments with single NPs and small assemblies (Supplementary Figs. 10 and 24).

We also investigated the global gene expression profiles in NSCs treated with $C_{30(\text{D})}S_5-C_{20(\text{L})}$ (Fig. 4a). The obvious differences with gene activation profiles in control cells and those that were CPL-illuminated with the polarity-optimized RRR-LL protocol are for *Map2*, *Taz*, *ROCK2* and *Mast1* (Fig. 4b). The upregulation of *Map2* and downregulation of *ROCK2* are of no surprise, because they are positively correlated with the differentiation of NSCs to neurons³⁰ and negatively associated with neurite growth³¹, respectively. The upregulation of *Mast1* is informative for deciphering the mechanism of CPL-accelerated differentiation, because this gene is positively associated with microtubules and the cytoskeleton³². Of particular interest, also, is the distinct upregulation of *YAP1* (Yes-associated protein 1) and *TAZ* (also known as *WWTR1*); both genes are directly and positively associated with activation of the mechanotransduction signalling pathway^{33–35} (Supplementary Table 2). The NSCs incorporating $C_{30(\text{D})}S_5-C_{20(\text{L})}$ exhibited the highest *YAP1* fluorescence intensity after RRR-LL rather than for other illumination protocols (Supplementary Fig. 26). We also

found that the mean fluorescence intensity of *YAP1* under RCP irradiation (13.5 ± 2.7) was higher than that obtained under LP (11.4 ± 3.0) or LCP light (9.3 ± 2.1)—that is, $\text{RCP} > \text{LP} > \text{LCP}$. This matches the polarization dependence of NSC differentiation (Supplementary Fig. 26). The positive relationship of *YAP1* with the CPL-accelerated NSC differentiation (Fig. 4a,b) is also supported by immunofluorescence staining.

Note that mechanical stimulation of the cells, such as cyclical stretching of substrates³⁶, were not utilized in our experimental protocols and the thermal expansion–contraction cycle is negligible for our illumination conditions. The illumination alone without nanoassemblies that might have caused cyclic mechanical deformations of the substrate under 50-Hz light did not accelerate NSC differentiation (Supplementary Fig. 8).

We investigated the possibility of cyclic mechanical tension applied directly to the cytoskeletal structure through NP assemblies. $C_{30}S_5-C_{20}$ nanoassemblies display an open branched geometry that can be easily entangled with one or more microtubules of the cytoskeleton. Previous data have indicated that CPL-illuminated multiparticle superstructures can generate forces sufficient to pull the assemblies together¹⁷. We thus carried out calculations importing the experimentally obtained $C_{30(\text{D})}S_5-C_{20(\text{L})}$ architecture into the COMSOL Multiphysics environment to evaluate the magnitude of plasmonic force possible for different CPL protocols. As an initial test validating this method, we calculated the CD spectrum of the $C_{30(\text{D})}S_5-C_{20(\text{L})}$ and found that it matched the experimental spectrum very well (Fig. 4c and Supplementary Fig. 27). Then, the total force, $\mathbf{F} = F_x\hat{x} + F_y\hat{y} + F_z\hat{z}$, acting on the $C_{30(\text{D})}S_5-C_{20(\text{L})}$ (64 different orientations were averaged) for LCP, LP and RCP illumination were calculated by integrating the Maxwell stress tensor. We found that the assembly exerted a substantially larger force under RCP ($1.0 \times 10^{-8} \text{ N}$) than under LCP ($1.1 \times 10^{-9} \text{ N}$) and LP ($8.5 \times 10^{-9} \text{ N}$). Note that the force for RCP is approximately nine times larger than for LCP, which can have much greater consequences than the total number of absorbed photons. In our case, the chiroplasmonic force is applied to the cytoskeleton with a laser repetition rate frequency of 50 Hz used for illumination. The relative magnitude of the force generated for the three polarizations— $\text{RCP} > \text{LP} > \text{LCP}$ —is consistent with the order of the acceleration of the differentiation for different polarizations (Fig. 4e and Supplementary Table 3). Note that the force in the range of 10 nN generated by a single $C_{30(\text{D})}S_5-C_{20(\text{L})}$ is sufficient to deform the nanoscale filaments in the cytoskeleton^{37–39} and, therefore, for intracellular mechanotransduction⁴⁰. Similar to optical tweezers⁴¹, the CPL illumination resulted in a periodic force transduced to the cytoskeleton and nucleus⁴² that is capable of accelerating NSC differentiation⁴³.

To investigate the mechanotransduction further, we carried out two-photon luminescence (TPL) imaging (Fig. 5a–c and Supplementary Fig. 28) and found that the nanoassemblies are entangled with α -actinin-1 protein in the cytoskeletal network^{44,45}. The fluorescence of α -actinin-1 was higher under RCP (45.8 ± 1.9) than LCP (32.1 ± 3.2) and LP (37.0 ± 2.8), as was confirmed by western blot analysis (Fig. 5d–f). This finding indicates that the development of the cytoskeleton can entangle more and more nanoassemblies in the course of our five-day differentiation protocol when NSCs are incubated with nanoassemblies every day (Methods).

Importantly, the RRR-LL and LLL-RR protocols were also tested for a different type of stem cell. The differentiation process and the polarization order corresponding to the RRR-LL and LLL-RR protocols were confirmed for human-bone-marrow mesenchymal stem cells after they were incubated with $C_{30(\text{D})}S_5-C_{20(\text{L})}$ or $C_{30(\text{L})}S_5-C_{20(\text{D})}$ (Supplementary Figs. 29 and 30).

Functionality of CPL-differentiated NSCs. The biological functionalities of the neurons obtained after CPL-accelerated differentiation of NSCs were tested in PrP-hApp/hPS1 double transgenic

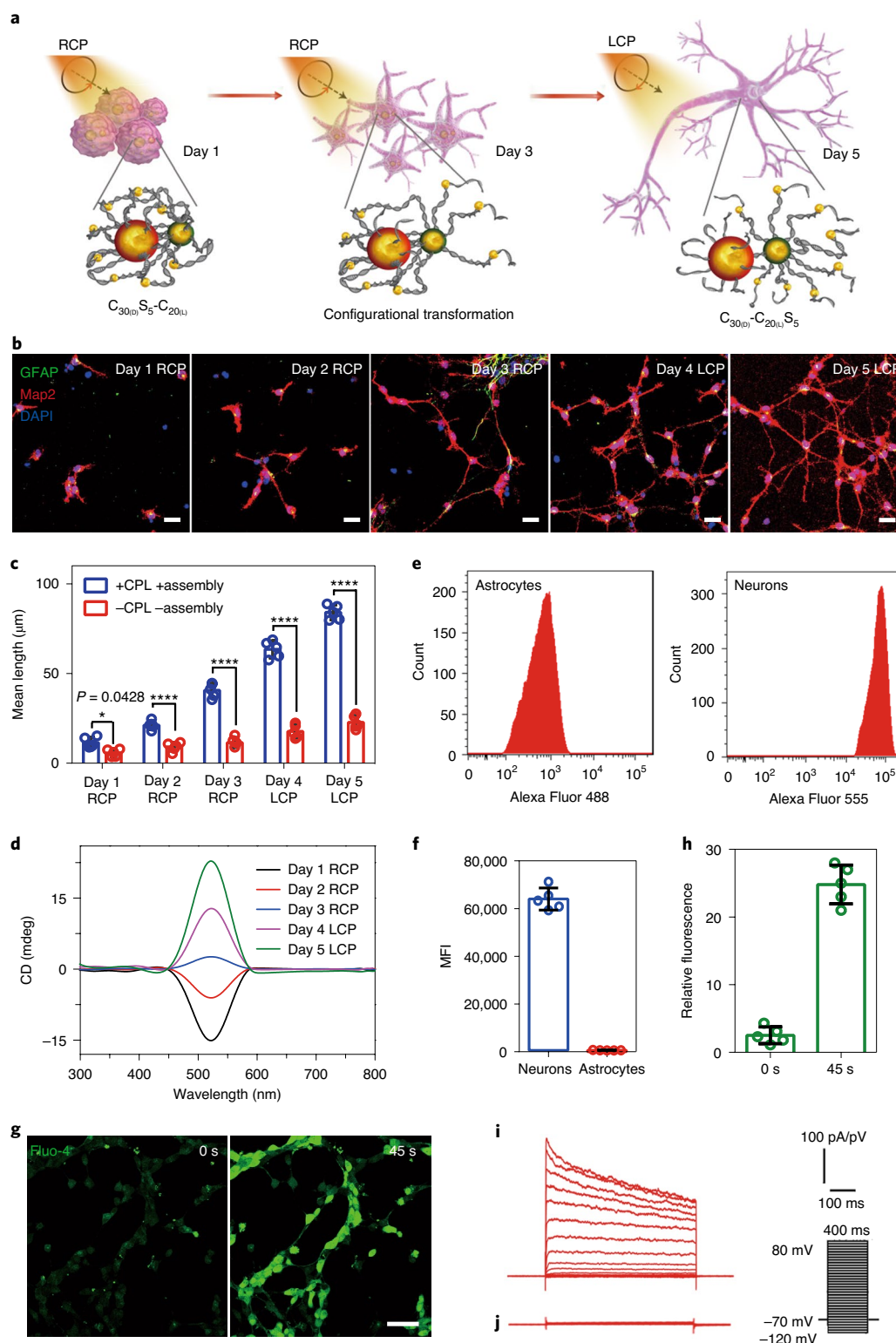


Fig. 3 | Differentiation of NSCs under CPL illumination. **a**, Schematic of differentiation of NSCs with CPL after daily incubation with $C_{30(0)}S_5-C_{20(L)}$ for five days. **b**, Confocal images of NSCs incubated with $C_{30(0)}S_5-C_{20(L)}$ for 4 h each day, and subsequently illuminated following the polarity-optimized CPL protocol (RRR-LL; 50 μ J per pulse, 50 Hz, 5 min) for five days; cells without nanoassemblies or CPL illumination were used as a control. Red, Map2 for mature neurons; blue, DAPI for nuclei; green, GFAP for astrocytes. Scale bars, 20 μ m. **c**, Mean lengths of neurites in differentiated NSCs. **d**, CD spectra of differentiated NSCs from day 1 to day 5. **e**, Detection of astrocytes and neurons by flow cytometry in differentiated NSCs cultured with $C_{30(0)}S_5-C_{20(L)}$ and illuminated following the RRR-LL protocol. (Alexa Fluor 488-labelled GFAP; Alexa Fluor 555-labelled Map2). **f**, MFI for the results in **e**. **g**, Ca^{2+} image of NSCs cultured with $C_{30(0)}S_5-C_{20(L)}$ and illuminated following the RRR-LL protocol after addition of 10 nM carbachol (agonist). Scale bar, 30 μ m. **h**, Relative fluorescence intensity of the Ca^{2+} image of NSCs in **g**. **i**, Representative voltage-dependent membrane potassium currents of NSCs cultured with $C_{30(0)}S_5-C_{20(L)}$ nanoassemblies and illuminated following the RRR-LL protocol (**i**) and NSCs illuminated following the RRR-LL protocol without $C_{30(0)}S_5-C_{20(L)}$ nanoassemblies incubation (**j**). * $P < 0.05$, **** $P < 0.0001$. Data are presented as mean \pm s.d. ($n = 5$).

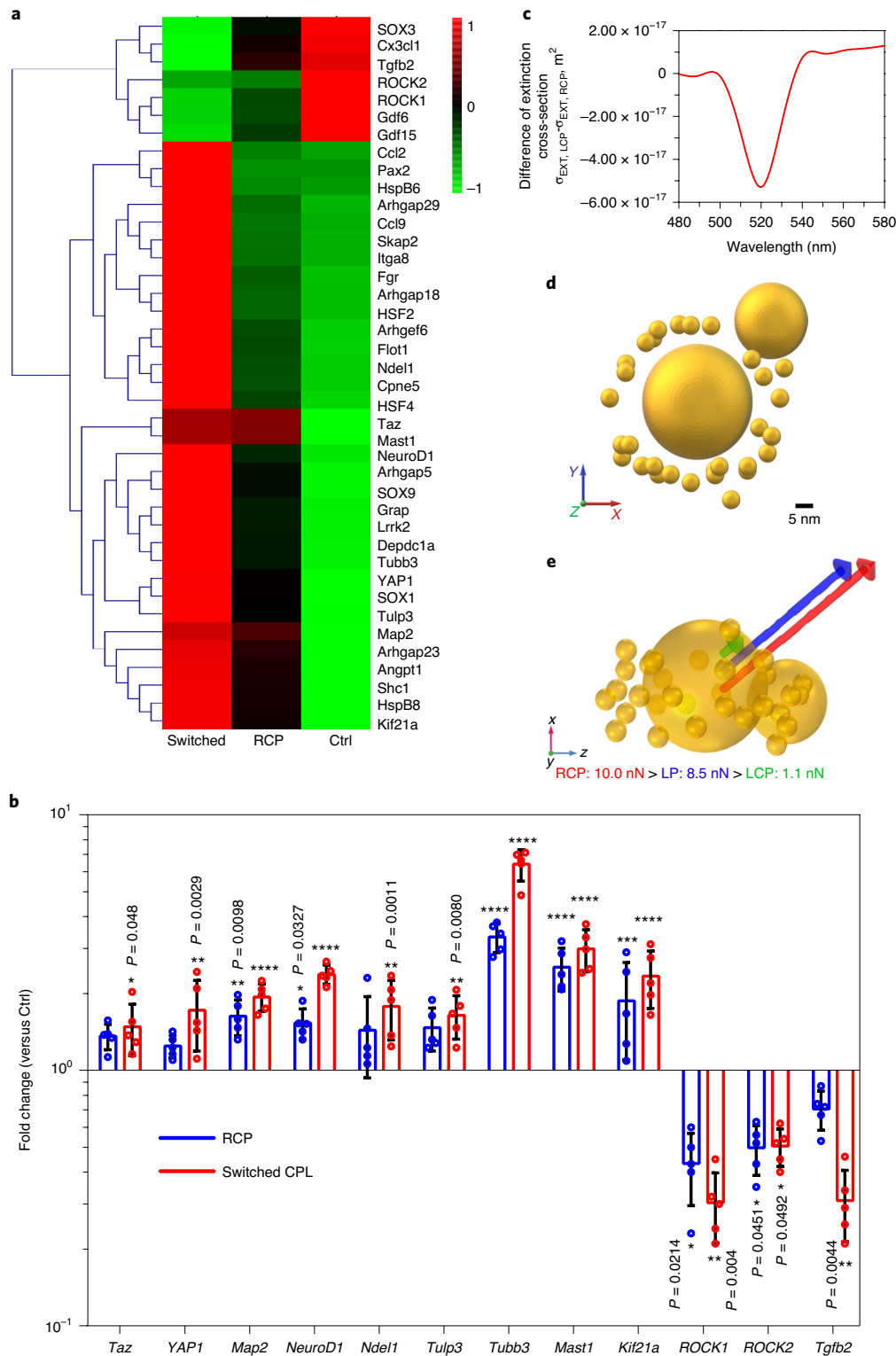


Fig. 4 | Mechanism of NSC differentiation after CPL irradiation. **a**, Global gene-expression pattern of transcription factors in NSCs incubated with PBS (Ctrl) or cultured with $C_{30(6)}S_5-C_{20(6)}$ and illuminated with the polarity-optimized CPL illumination protocol (RRR-LL) or the continuous RCP sequence (RRRRR) (50 μ J per pulse, 50 Hz, 5 min) for five days. **b**, The differentially expressed genes from the heatmap results are expressed as fold change compared with levels in Ctrl (five technical pools of 1×10^5 cells were averaged per biological replicate). * $P < 0.05$, ** $P < 0.01$, *** $P < 0.001$, **** $P < 0.0001$. **c**, Calculated CD spectrum (difference in the extinction cross-section under LCP and RCP) for the chiral Au NP assembly ($C_{30(6)}S_5-C_{20(6)}$) model. **d**, $C_{30(6)}S_5-C_{20(6)}$ nanoassembly model for the electromagnetic computation. The incident beam propagates in the z direction. **e**, Averaged mechanical forces experienced by the $C_{30(6)}S_5-C_{20(6)}$ under three different polarizations at a wavelength of 520 nm. The volume arrow plots (red, blue and green) are proportional to the magnitude of the mechanical forces under RCP, LP and LCP, respectively. The incident beam propagates in the z direction. Note that the force vector should be interpreted based on the incident beam direction. The orientation of the multiparticle assembly displaced in this figure is just one of 64 different orientations calculated.

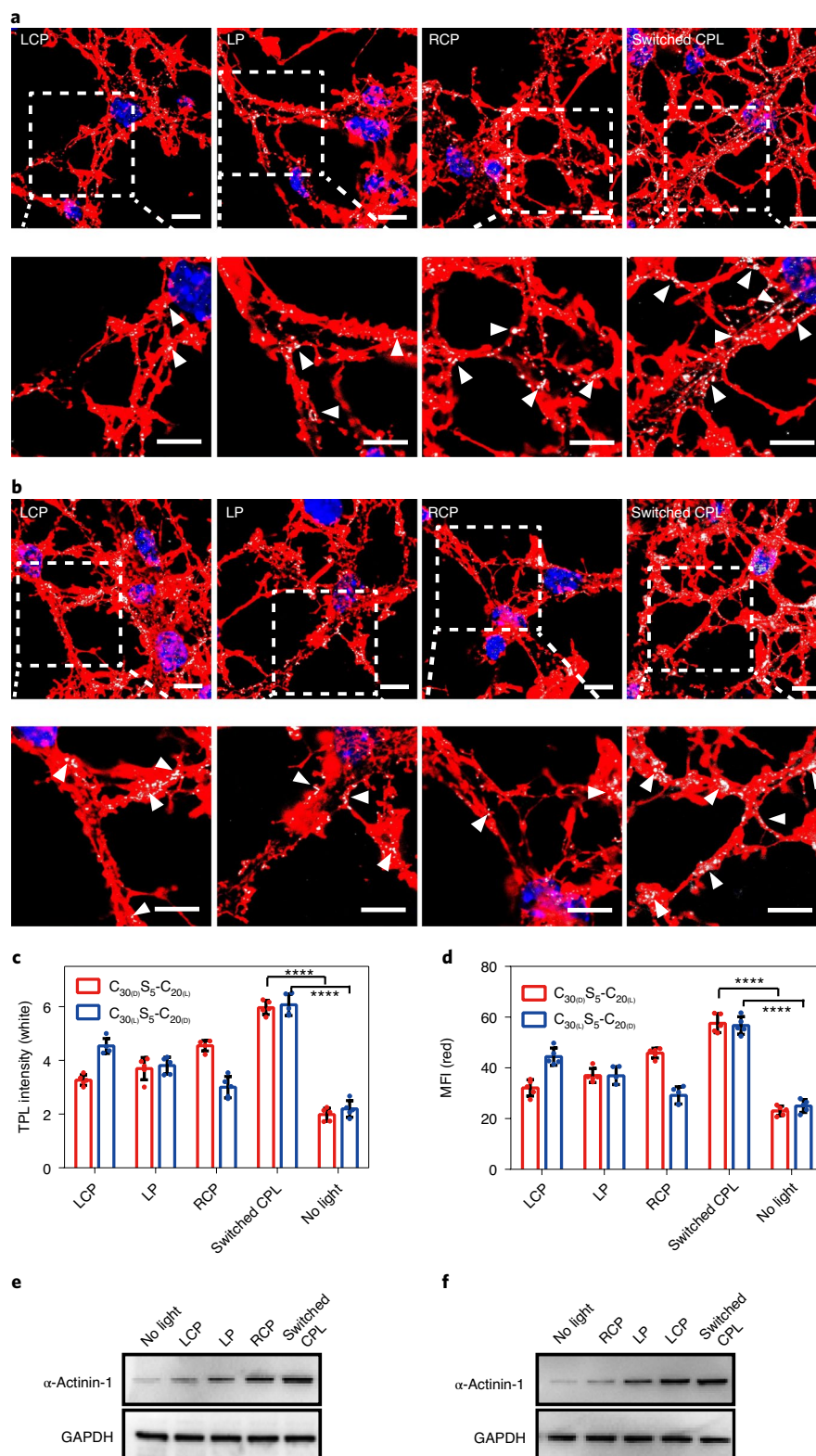


Fig. 5 | Characterization of the chiral nanoassemblies entangled with cytoskeleton under CPL illumination. a,b, Two-photon luminescence images of α -actinin-1 for cytoskeleton in NSCs after incubation with $C_{30(L)}S_5-C_{20(L)}$ (**a**) or $C_{30(L)}S_5-C_{20(R)}$ (**b**) for 4 h each day and then exposed to no light, RCP, LP, LCP or the polarity-optimized CPL illumination protocol (RRR-LL for $C_{30(L)}S_5-C_{20(L)}$; LLL-RR for $C_{30(L)}S_5-C_{20(R)}$) ($50 \mu\text{J}$ per pulse, 50 Hz, 5 min) for five days. Red, α -actinin-1 for cytoskeleton; white, $C_{30(L)}S_5-C_{20(L)}$ or $C_{30(L)}S_5-C_{20(R)}$ nanoassemblies (white arrowheads); blue, DAPI for the nuclei. Scale bars, $10 \mu\text{m}$. **c**, TPL intensity of $C_{30(L)}S_5-C_{20(L)}$ or $C_{30(L)}S_5-C_{20(R)}$ on the cytoskeleton. The mean TPL intensities of $C_{30(L)}S_5-C_{20(L)}$ on the cytoskeleton under RCP, LP and LCP illumination are 4.5 ± 0.20 , 3.7 ± 0.41 and 3.3 ± 0.20 , respectively. **d**, MFI of α -actinin-1 of differentiated NSCs. **e,f**, Western blot analysis for α -actinin-1 in differentiated NSCs after incubation with $C_{30(L)}S_5-C_{20(L)}$ (**e**) or $C_{30(L)}S_5-C_{20(R)}$ (**f**) and illuminated with different CPL. GAPDH acts as a control. **** $P < 0.0001$. Original western blot images are provided in Supplementary Fig. 38a–d. Data are presented as mean \pm s.d. ($n = 5$).

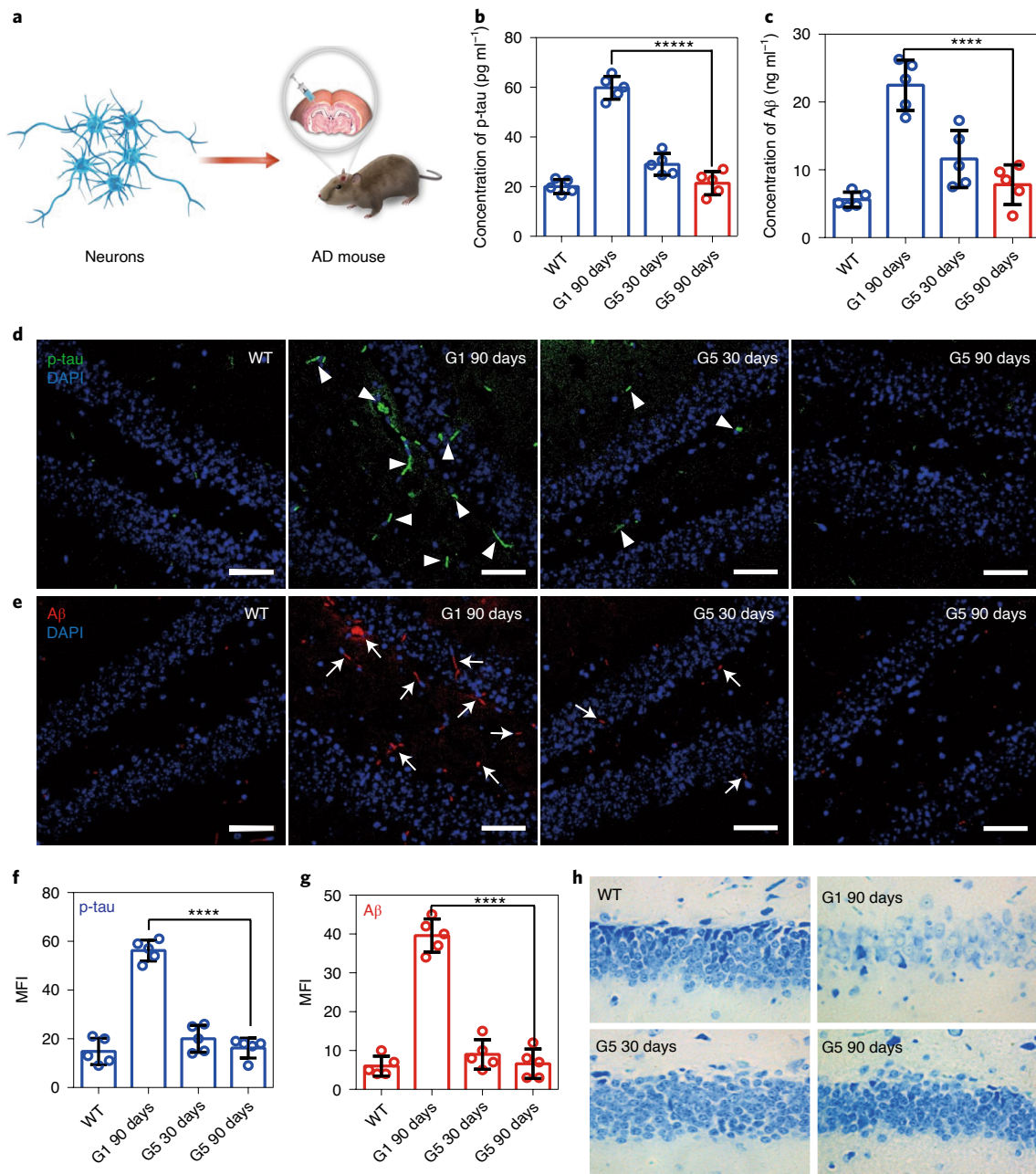


Fig. 6 | In vivo AD therapy through CPL-accelerated NSCs. **a**, Schematic of in vivo AD therapy through the injection of differentiated NSCs after different treatments. The nanoassemblies were removed from implanted CPL-differentiated NSCs by post-illumination culture time during which they cleared from the cells. The nanoassemblies exhibited no cytotoxicity after injection into AD mice (Supplementary Figs. 33 and 34). **b,c**, p-tau (**b**) and Aβ (**c**) concentrations in cerebrospinal fluid of AD mice after G1 or G5 treatment (Methods). **d,e**, Immunofluorescence of p-tau (white arrowheads) (**d**) and Aβ (white arrows) (**e**) in the hippocampus of AD mice after G1 or G5 treatment. Scale bars, 50 μm. **f,g**, Mean fluorescence intensity of p-tau (**f**) and Aβ (**g**) in the hippocampus after G1 or G5 treatment. **h**, Nissl staining of neuro cells in the brains (hippocampus) of AD mice with G1 or G5 treatment. ****P < 0.0001. Data are presented as mean ± s.d. (n = 5). Animal groups: WT, wild-type mice without any treatment; G1, NSCs incubated with PBS; G5, NSCs incubated with C₃₀₍₀₎S₅-C₂₀₍₄₎ illuminated using the polarity-optimized CPL illumination protocol (RRR-LL).

mice (2xTg-AD) serving as an animal model for Alzheimer's disease (AD). A distinct improvement of the cognitive ability of AD mice was observed within the 90-day observation period after treatment with the CPL-differentiated NSCs (Fig. 7e–g and Supplementary Figs. 31 and 32). Note that implanted cells do not contain any nanoassemblies after 10 days of post-illumination culture time (Supplementary Fig. 33).

Both hallmarks of AD, the amyloid-β (Aβ) and hyperphosphorylated tau (p-tau) proteins^{46,47}, extracted from the cerebrospinal fluid

(CSF) of AD mice, were reduced by more than 70% (Fig. 6b,c) after implantation of the NSCs that had been CPL-differentiated in the polarity-optimized protocol. Quite remarkably, the concentrations of these toxic proteins were restored to the levels in WT mice. Immunohistochemical and immunofluorescence analyses also showed dramatic reductions in Aβ and p-tau compared to PBS-treated AD mice (Figs. 6d–g and 7a,b).

Bromodeoxyuridine (BrdU) labelling of newly dividing cells demonstrated their differentiation into neurons based on doublecortin

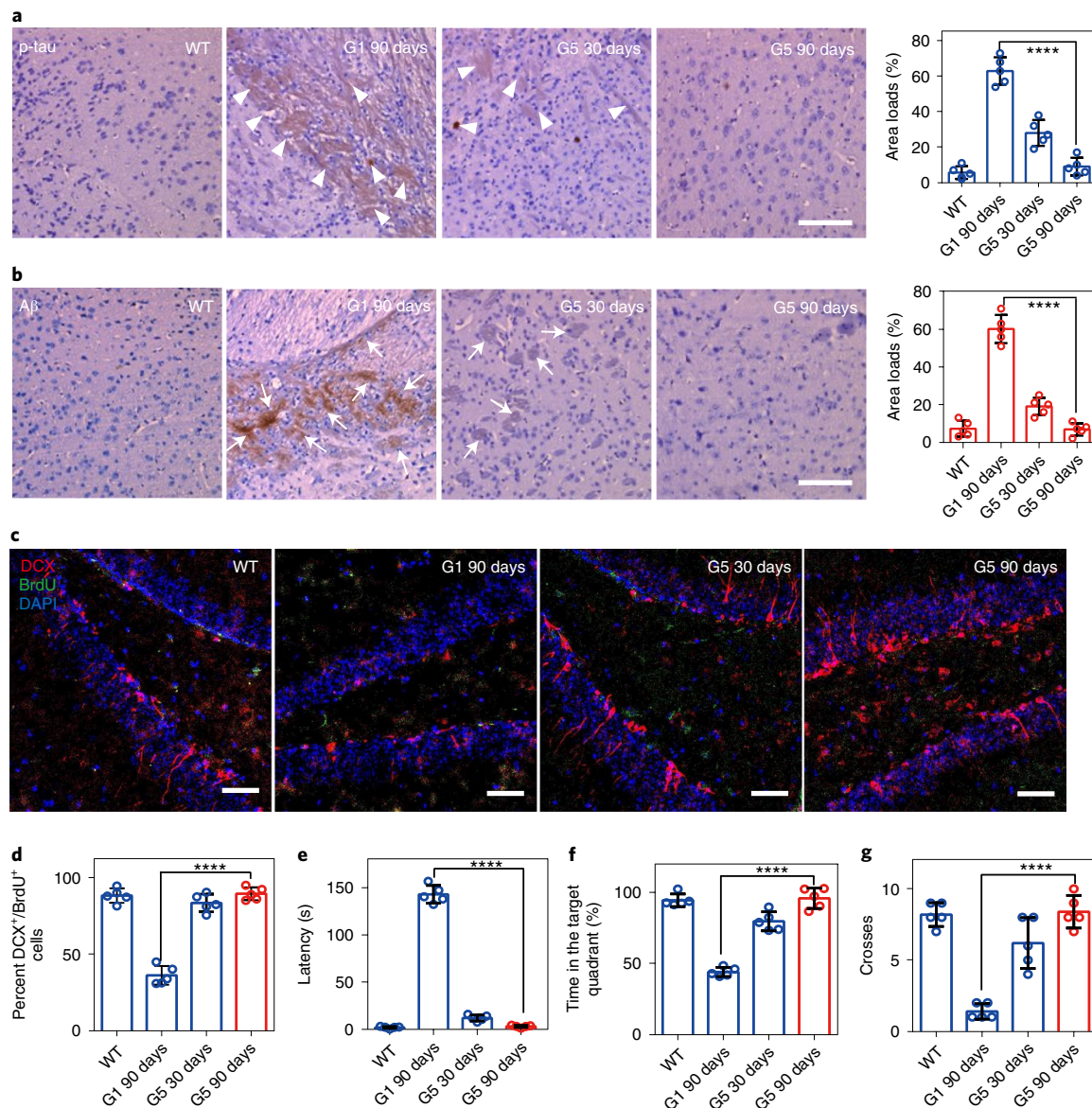


Fig. 7 | Restoration of neurons and cognitive ability of AD mice by CPL-accelerated NSCs. **a,b**, Representative immunostaining of hippocampal sections for p-tau (white arrowheads) (**a**) and Aβ (white arrows) (**b**) protein aggregates of AD mice after G1 or G5 treatment. Scale bars, 50 μm. The graphs show the results of quantitative analysis of p-tau and Aβ loads in the brains (hippocampus) after different treatments. **c**, Representative hippocampal section images of AD mice with G1 or G5 treatment, immunostained for DCX (red) to label immature neurons, BrdU (green) to label dividing cells and DAPI (blue) to stain nuclei. Scale bars, 50 μm. **d**, Quantification of the overall fraction of newborn hippocampal cells in **c** that underwent neuronal differentiation using stereological estimation. **e**, The latent period to find the target quadrant in a water maze of WT and AD mice after injection of NSCs with different treatments. **f**, The time in the target quadrant for the WT and AD mice with different treatments. **g**, The crosses times in the target quadrant of the WT and AD mice after injection of NSCs with different treatment. **** $P < 0.0001$. Data are presented as mean \pm s.d. ($n = 5$). Animal groups: WT, wild-type mice without any treatment; G1, NSCs incubated with PBS; G5, NSCs incubated with $C_{30(n)}S_5-C_{20(l)}$ illuminated with the polarity-optimized CPL illumination protocol (RRR-LL).

(DCX) labelling in hippocampus (Fig. 7c,d). Nissl staining of the hippocampus also showed that the nuclei of the neurons were intact and they had increased in number compared with the group where NSCs were incubated with PBS (Fig. 6h). Treatments of AD mice with NSCs cultured under (1) LP irradiation without $C_{30(n)}S_5-C_{20(l)}$ incubation, (2) NSCs incubated with $C_{30(n)}S_5-C_{20(l)}$ without CPL and (3) AD mice injected with $C_{30(n)}S_5-C_{20(l)}$ with CPL illumination showed no symptomatic improvement (Supplementary Figs. 35–37).

Discussion

The differentiation of NSCs into functional neurons is accelerated by circularly polarized photons when chiral nanoassemblies

are entangled with the cytoskeleton of stem cells. The mechanism of this phenomenon includes three essential elements: (1) chiroptically active NP assemblies enter the cells and change their conformation, enmeshing the DNA-bridged NPs with the actin network; (2) CPL exerts a polarization-dependent force on the nanoassemblies and, thus, on the nanofibres; (3) periodic mechanical deformation of the cytoskeleton under 50-Hz pulsed light stimulates NSC differentiation into neuronal phenotypes. The large differences in neurite length, global gene expression analysis and differentiation markers and the large difference between RCP, LCP and LP light illumination protocols verify the mechanism and demonstrate that circular polarization can be

utilized to direct stem cell development along a desirable neuronal pathway.

Implantation of CPL-differentiated NSCs substantially reduced the p-tau and A β protein contents in AD mice, leading to a recovery in their pathologic behaviour. Assessing the future translational potential of this study, we need to point out that DNA-bridged constructs are not the only path to take in engineering chiral nanoassemblies. Because we know now the mechanism of the phenomenon, multiple NP constructs with appropriate size and optical activity can be engineered using other flexible bridges. The key requirements for these nanoassemblies are chirality, flexibility and biocompatibility. Numerous polymers that can be conjugated to gold NPs can result in such nanoassemblies²³. Although entangling of the nanoassemblies with actin nanofibres was attained in this work via conformational change inside cells, the tight binding to the cytoskeleton can also be accomplished by other means, for example by using traditional cytoskeleton markers. Our findings provide a mechanistic framework for further exploration of the biological effects of CPL for different types of cell and their biomedical applications.

Methods

Cell culture. Mouse NSCs were cultured in complete medium consisting of mouse neural stem cell basal medium, penicillin-streptomycin, glutamine, heparin, basic fibroblast growth factor (bFGF), epidermal growth factor (EGF) and B27. The cells were maintained at 37 °C in a humidified atmosphere of 5% CO₂ for 24 h. The cells were then seeded onto poly-D-lysine/laminin-coated glass coverslips and allowed to adhere before differentiation. The complete medium was stable for up to four weeks when stored in the dark at 4 °C.

CPL-accelerated NSC differentiation. NSCs were seeded on the poly-D-lysine/laminin-coated six-well plate in an adhesion state at a density of 1×10^6 cells per well in 1 ml of culture medium for 24 h. After the cells had adhered to the substrate, final concentrations of 1 μ M retinoic acid (RA) and 2 μ g ml⁻¹ siSOX9 were added to the cell medium, and the cells were incubated for 12 h. The cells were then incubated with fresh culture medium containing 50 nM nanoassemblies for 4 h, and then washed three times to remove excess particles, supplemented with fresh medium and irradiated with CPL for 5 min; this process continued for five days.

CD detection. The concentration of the nanoassemblies was chosen to be 50 nM for all CD measurements in the buffer, and the light path was 10 mm. For the intracellular CD test, differentiated and adherent cells were collected in PBS suspension for CD measurements. The light path of the measurement cell was 10 mm.

Animal models. Ten-month-old PrP-hApp/hPS1 double transgenic mice (2xTg-AD, PrP-hApp/hPS1 transgenic mice expressing a chimaeric mouse/human amyloid precursor protein (APP) containing the Swedish K595N/M596L mutations and human PS1 with the deltaE9 mutation) were stereotactically injected with 1×10^6 NSCs in 5 μ l of cold PBS. The injection coordinates, relative to the bregma, were as follows: anteroposterior, -1.70 mm; mediolateral, 1.50 mm; dorsoventral, -1.50 mm. All animal experiments were approved by the Committee on Animal Welfare of Jiangnan University: group 1 (G1), NSCs incubated with PBS (control); G2, NSCs incubated with C_{30(n)}S₅-C_{20(l)} under LCP; G3, NSCs incubated with C_{30(n)}S₅-C_{20(l)} under LP; G4, NSCs incubated with C_{30(n)}S₅-C_{20(l)} under RCP; G5, NSCs incubated with C_{30(n)}S₅-C_{20(l)} under the polarity-optimized CPL protocol (first three days RCP and last two days LCP, RRR-LL); G6, NSCs incubated with C_{30(n)}S₅-C_{20(l)} under the switched CPL protocol (first two days RCP and last three days LCP, RR-LLL); G7: NSCs incubated with C_{30(n)}S₅-C_{20(l)} under the switched CPL protocol (first four days RCP and last day LCP, RRRR-L); G8, NSCs incubated with C_{30(n)}S₅-C_{20(l)} without CPL; G9, NSCs incubated without C_{30(n)}S₅-C_{20(l)} and under LP; G10, mice injected with C_{30(n)}S₅-C_{20(l)} directly and under the polarity-optimized CPL protocol (RRR-LL; 5 min each day) for five days.

Animal studies. 2xTg-AD mice were randomly selected for the experimental groups (at least three mice per group) and stereotactically injected with 1×10^6 NSCs under different differentiated conditions. NSC-treated mice were monitored daily, and animals with poor post-surgical recovery or signs such as dyspnoea and inactivity were also excluded. This occurred in ~3% of cases. Behaviour and image analyses were blinded and performed by independent investigators. Histological analyses were blinded and performed by an independent investigator.

Statistical analysis. All data are presented as mean \pm s.d. For each experimental series, at least three replicates ($n=3$) were performed unless otherwise stated. For

many experimental series at least five independent experiments were carried out; n values given in the figure legends indicate the number of independent experiments performed or the number of mice. Group differences were considered statistically significant when $P < 0.05$ (* $P < 0.05$, ** $P < 0.01$, *** $P < 0.001$, **** $P < 0.0001$), and an analysis of variance test was used for multicomponent comparisons.

Reporting Summary. Further information on research design is available in the Nature Research Reporting Summary linked to this article.

Data availability

The data supporting the findings of this study are available within the paper and its Supplementary Information. The raw data are available from figshare with the identifier <https://doi.org/10.6084/m9.figshare.12931874>.

Received: 17 October 2019; Accepted: 23 September 2020;
Published online: 26 October 2020

References

- Paviolo, C. et al. Laser exposure of gold nanorods can increase neuronal cell outgrowth. *Biotechnol. Bioeng.* **110**, 2277–2291 (2013).
- Baba, J. S., Chung, J. R., DeLaughter, A. H., Cameron, B. D. & Cote, G. L. Development and calibration of an automated Mueller matrix polarization imaging system. *J. Biomed. Opt.* **7**, 341–349 (2002).
- Funck, T., Nicoli, F., Kuzyk, A. & Liedl, T. Sensing picomolar concentrations of RNA using switchable plasmonic chirality. *Angew. Chem. Int. Ed.* **57**, 13495–13498 (2018).
- Hendry, E. et al. Ultrasensitive detection and characterization of biomolecules using superchiral fields. *Nat. Nanotechnol.* **5**, 783–787 (2010).
- Chen, W. et al. Nanoparticle superstructures made by polymerase chain reaction: collective interactions of nanoparticles and a new principle for chiral materials. *Nano Lett.* **9**, 2153–2159 (2009).
- Zhao, X. et al. Tuning the interactions between chiral plasmonic films and living cells. *Nat. Commun.* **8**, 2007 (2017).
- Patel, M., Moon, H. J., Hong, J. H. & Jeong, B. Chiro-optical modulation for NURR1 production from stem cells. *ACS Chem. Neurosci.* **8**, 1455–1458 (2017).
- Morrow, S. M., Bisette, A. J. & Fletcher, S. P. Transmission of chirality through space and across length scales. *Nat. Nanotechnol.* **12**, 410–419 (2017).
- Vestler, D. et al. Circular dichroism enhancement in plasmonic nanorod metamaterials. *Opt. Express* **26**, 17841–17848 (2018).
- Govan, J. & Gun'ko, Y. K. in *Nanoscience Vol. 3*, 1–30 (Royal Society of Chemistry, 2016).
- Auguie, B., Alonso-Gómez, J. L., Guerrero-Martínez, A. & Liz-Marzán, L. M. Fingers crossed: optical activity of a chiral dimer of plasmonic nanorods. *J. Phys. Chem. Lett.* **2**, 846–851 (2011).
- Sun, M. et al. Intracellular localization of nanoparticle dimers by chirality reversal. *Nat. Commun.* **8**, 1847 (2017).
- Ma, W. et al. Chiral inorganic nanostructures. *Chem. Rev.* **117**, 8041–8093 (2017).
- Zhou, L. A. et al. Quantifying hot carrier and thermal contributions in plasmonic photocatalysis. *Science* **362**, 69–72 (2018).
- Sun, M. Z. et al. Site-selective photoinduced cleavage and profiling of DNA by chiral semiconductor nanoparticles. *Nat. Chem.* **10**, 821–830 (2018).
- Li, S. et al. Single- and multi-component chiral supraparticles as modular enantioselective catalysts. *Nat. Commun.* **10**, 4826 (2019).
- Kim, J.-Y. et al. Assembly of gold nanoparticles into chiral superstructures driven by circularly polarized light. *J. Am. Chem. Soc.* **141**, 11739–11744 (2019).
- Valev, V. K. et al. Nanostripe length dependence of plasmon-induced material deformations. *Opt. Lett.* **38**, 2256–2258 (2013).
- Laramy, C. R., O'Brien, M. N. & Mirkin, C. A. Crystal engineering with DNA. *Nat. Rev. Mater.* **4**, 201–224 (2019).
- Chen, G. et al. Regioselective surface encoding of nanoparticles for programmable self-assembly. *Nat. Mater.* **18**, 169–174 (2019).
- Leung, K., Chakraborty, K., Saminathan, A. & Krishnan, Y. A DNA nanomachine chemically resolves lysosomes in live cells. *Nat. Nanotechnol.* **14**, 176–183 (2019).
- Zhang, Q. F. et al. Unraveling the origin of chirality from plasmonic nanoparticle-protein complexes. *Science* **365**, 1475–1478 (2019).
- Lu, D. R., Zhou, J. J., Chen, Y. H., Ma, J. L. & Duan, H. W. Self-assembly of polymer-coated plasmonic nanocrystals: from synthetic approaches to practical applications. *Macromol. Rapid Commun.* **40**, 1800613 (2019).
- Ben-Moshe, A., Maoz, B., Govorov, A. O. & Markovich, G. Chirality and chiroptical effects in inorganic nanocrystal systems with plasmon and exciton resonances. *Chem. Soc. Rev.* **42**, 7028–7041 (2013).
- Verma, A. et al. Surface-structure-regulated cell-membrane penetration by monolayer-protected nanoparticles. *Nat. Mater.* **7**, 588–595 (2008).
- Samanta, D., Ebrahimi, S. B. & Mirkin, C. A. Nucleic-acid structures as intracellular probes for live cells. *Adv. Mater.* **32**, 1901743 (2019).

27. Wang, Z. et al. Bioinspired nanocomplex for spatiotemporal imaging of sequential mRNA expression in differentiating neural stem cells. *ACS Nano* **8**, 12386–12396 (2014).
28. Calza, L., Fernandez, M., Giuliani, A., Aloe, L. & Giordano, L. Thyroid hormone activates oligodendrocyte precursors and increases a myelin-forming protein and NGF content in the spinal cord during experimental allergic encephalomyelitis. *Proc. Natl Acad. Sci. USA* **99**, 3258–3263 (2002).
29. Solanki, A., Shah, S., Yin, P. T. & Lee, K.-B. Nanotopography-mediated reverse uptake for siRNA delivery into neural stem cells to enhance neuronal differentiation. *Sci. Rep.* **3**, 1553 (2013).
30. Johnson, G. V. W. & Jope, R. S. The role of microtubule-associated protein-2 (Map-2) in neuronal growth, plasticity and degeneration. *J. Neurosci. Res.* **33**, 505–512 (1992).
31. Gu, H., Yu, S. P., Gutekunst, C.-A., Gross, R. E. & Wei, L. Inhibition of the Rho signaling pathway improves neurite outgrowth and neuronal differentiation of mouse neural stem cells. *Int. J. Physiol. Pathophysiol. Pharmacol.* **5**, 11–20 (2013).
32. Garland, P., Quraishi, S., French, P. & O'Connor, V. Expression of the MAST family of serine/threonine kinases. *Brain Res.* **1195**, 12–19 (2008).
33. Dupont, S. et al. Role of YAP/TAZ in mechanotransduction. *Nature* **474**, 179–183 (2011).
34. Brusatin, G., Panciera, T., Gandin, A., Citron, A. & Piccolo, S. Biomaterials and engineered microenvironments to control YAP/TAZ-dependent cell behaviour. *Nat. Mater.* **17**, 1063–1075 (2018).
35. Xue, X. F. et al. Mechanics-guided embryonic patterning of neuroectoderm tissue from human pluripotent stem cells. *Nat. Mater.* **17**, 633–641 (2018).
36. Cui, Y. et al. Cyclic stretching of soft substrates induces spreading and growth. *Nat. Commun.* **6**, 6333 (2015).
37. Asbury, C. L., Gestaut, D. R., Powers, A. F., Franck, A. D. & Davis, T. N. The Dam1 kinetochore complex harnesses microtubule dynamics to produce force and movement. *Proc. Natl Acad. Sci. USA* **103**, 9873–9878 (2006).
38. Kreplak, L., Herrmann, H. & Aebi, U. Tensile properties of single desmin intermediate filaments. *Biophys. J.* **94**, 2790–2799 (2008).
39. Guolla, L., Bertrand, M., Haase, K. & Pelling, A. E. Force transduction and strain dynamics in actin stress fibres in response to nanonewton forces. *J. Cell Sci.* **125**, 603–613 (2012).
40. Shafir, Y. & Forgacs, G. Mechanotransduction through the cytoskeleton. *Am. J. Physiol. Cell Physiol.* **282**, C479–C486 (2002).
41. Juan, M. L., Righini, M. & Quidant, R. Plasmon nano-optical tweezers. *Nat. Photon.* **5**, 349–356 (2011).
42. Karafyllidis, I. G. & Lagoudas, D. C. Microtubules as mechanical force sensors. *Biosystems* **88**, 137–146 (2007).
43. Fletcher, D. A. & Mullins, R. D. Cell mechanics and the cytoskeleton. *Nature* **463**, 485–492 (2010).
44. Torii, T. et al. Arf6 guanine-nucleotide exchange factor, cytohesin-2, interacts with actinin-1 to regulate neurite extension. *Cell. Signal.* **24**, 1872–1882 (2012).
45. Tee, Y. H. et al. Cellular chirality arising from the self-organization of the actin cytoskeleton. *Nat. Cell Biol.* **17**, 445–457 (2015).
46. Da Mesquita, S. et al. Functional aspects of meningeal lymphatics in ageing and Alzheimer's disease. *Nature* **560**, 185–191 (2018).
47. Rice, H. C. et al. Secreted amyloid- β precursor protein functions as a GABABR1a ligand to modulate synaptic transmission. *Science* **363**, eaao4827 (2019).

Acknowledgements

This work is financially supported by the National Natural Science Foundation of China (grant nos. 21925402, 51802125 and 21631005). A part of this work (from N.A.K. and J.-Y.K.) was supported by NSF projects NSF 1463474, NSF 1566460 and DoD W911NF-10-1-0518.

Author contributions

H.K., N.A.K. and C.X. conceived the project and designed the experiments. A.Q. and M.S. were responsible for cell and animal experiments. J.-Y.K. carried out the electromagnetic calculations. L.X. and C.H. carried out the assembly synthesis. W.M. and X.W. were responsible for spectroscopic measurements. H.K. and N.A.K. conceptualized the work. C.X. and H.K. supervised the study. H.K., N.A.K. and C.X. analysed the results and wrote the manuscript. X.L., H.K., N.A.K. and C.X. discussed the results and commented on the manuscript.

Competing interests

The authors declare no competing interests.

Additional information

Supplementary information is available for this paper at <https://doi.org/10.1038/s41551-020-00634-4>.

Correspondence and requests for materials should be addressed to H.K., N.A.K. or C.X.

Reprints and permissions information is available at www.nature.com/reprints.

Publisher's note Springer Nature remains neutral with regard to jurisdictional claims in published maps and institutional affiliations.

© The Author(s), under exclusive licence to Springer Nature Limited 2020

Reporting Summary

Nature Research wishes to improve the reproducibility of the work that we publish. This form provides structure for consistency and transparency in reporting. For further information on Nature Research policies, see our [Editorial Policies](#) and the [Editorial Policy Checklist](#).

Statistics

For all statistical analyses, confirm that the following items are present in the figure legend, table legend, main text, or Methods section.

n/a Confirmed

- | | | |
|-------------------------------------|-------------------------------------|--|
| <input type="checkbox"/> | <input checked="" type="checkbox"/> | The exact sample size (n) for each experimental group/condition, given as a discrete number and unit of measurement |
| <input type="checkbox"/> | <input checked="" type="checkbox"/> | A statement on whether measurements were taken from distinct samples or whether the same sample was measured repeatedly |
| <input type="checkbox"/> | <input checked="" type="checkbox"/> | The statistical test(s) used AND whether they are one- or two-sided
<i>Only common tests should be described solely by name; describe more complex techniques in the Methods section.</i> |
| <input type="checkbox"/> | <input checked="" type="checkbox"/> | A description of all covariates tested |
| <input type="checkbox"/> | <input checked="" type="checkbox"/> | A description of any assumptions or corrections, such as tests of normality and adjustment for multiple comparisons |
| <input type="checkbox"/> | <input checked="" type="checkbox"/> | A full description of the statistical parameters including central tendency (e.g. means) or other basic estimates (e.g. regression coefficient) AND variation (e.g. standard deviation) or associated estimates of uncertainty (e.g. confidence intervals) |
| <input type="checkbox"/> | <input checked="" type="checkbox"/> | For null hypothesis testing, the test statistic (e.g. F , t , r) with confidence intervals, effect sizes, degrees of freedom and P value noted
<i>Give P values as exact values whenever suitable.</i> |
| <input checked="" type="checkbox"/> | <input type="checkbox"/> | For Bayesian analysis, information on the choice of priors and Markov chain Monte Carlo settings |
| <input checked="" type="checkbox"/> | <input type="checkbox"/> | For hierarchical and complex designs, identification of the appropriate level for tests and full reporting of outcomes |
| <input type="checkbox"/> | <input checked="" type="checkbox"/> | Estimates of effect sizes (e.g. Cohen's d , Pearson's r), indicating how they were calculated |

Our web collection on [statistics for biologists](#) contains articles on many of the points above.

Software and code

Policy information about [availability of computer code](#)

Data collection Gatan Microscopy Suite Software, Lieca LAS AF Lite, Living Image, Imaging Lab, Chirascan.

Data analysis OriginPro 8.5, Microsoft excel.

For manuscripts utilizing custom algorithms or software that are central to the research but not yet described in published literature, software must be made available to editors and reviewers. We strongly encourage code deposition in a community repository (e.g. GitHub). See the Nature Research [guidelines for submitting code & software](#) for further information.

Data

Policy information about [availability of data](#)

All manuscripts must include a [data availability statement](#). This statement should provide the following information, where applicable:

- Accession codes, unique identifiers, or web links for publicly available datasets
- A list of figures that have associated raw data
- A description of any restrictions on data availability

The data supporting the findings of this study are available within the paper and its Supplementary Information. The raw data are available from figshare with the identifier <https://doi.org/10.6084/m9.figshare.12931874>.

Field-specific reporting

Please select the one below that is the best fit for your research. If you are not sure, read the appropriate sections before making your selection.

☒ Life sciences ☐ Behavioural & social sciences ☐ Ecological, evolutionary & environmental sciences

For a reference copy of the document with all sections, see [nature.com/documents/nr-reporting-summary-flat.pdf](https://www.nature.com/documents/nr-reporting-summary-flat.pdf)

Life sciences study design

All studies must disclose on these points even when the disclosure is negative.

Sample size	Sample sizes were estimated on the basis of previous experience with a similar setup. For the cell experiments, at least 1 million cells were collected for each sample. Statistics were derived when at least three independent samples were analyzed. Experiments involving mice were divided into 15 groups, with at least three animals analysed for each group.
Data exclusions	No data were excluded from the analyses.
Replication	For each experiment and condition, at least three independent technical replicates were performed. All observations reported in the manuscript were reproducible.
Randomization	Mice were randomly selected and divided into different groups, with each group containing at least three mice.
Blinding	The investigators were blinded to group allocation during data collection and analysis.

Reporting for specific materials, systems and methods

We require information from authors about some types of materials, experimental systems and methods used in many studies. Here, indicate whether each material, system or method listed is relevant to your study. If you are not sure if a list item applies to your research, read the appropriate section before selecting a response.

Materials & experimental systems

n/a	Involved in the study
<input type="checkbox"/>	<input checked="" type="checkbox"/> Antibodies
<input type="checkbox"/>	<input checked="" type="checkbox"/> Eukaryotic cell lines
<input checked="" type="checkbox"/>	<input type="checkbox"/> Palaeontology and archaeology
<input type="checkbox"/>	<input checked="" type="checkbox"/> Animals and other organisms
<input checked="" type="checkbox"/>	<input type="checkbox"/> Human research participants
<input checked="" type="checkbox"/>	<input type="checkbox"/> Clinical data
<input checked="" type="checkbox"/>	<input type="checkbox"/> Dual use research of concern

Methods

n/a	Involved in the study
<input checked="" type="checkbox"/>	<input type="checkbox"/> ChIP-seq
<input type="checkbox"/>	<input checked="" type="checkbox"/> Flow cytometry
<input checked="" type="checkbox"/>	<input type="checkbox"/> MRI-based neuroimaging

Antibodies

Antibodies used

Mouse monoclonal anti-Map2 antibody (clone: AP18; MA5-12826) was purchased from Thermo Fisher (IF, Flow); Rabbit polyclonal anti-GFAP antibody (PA5-16291) was purchased from Thermo Fisher (IF, Flow); Goat anti-Rabbit IgG (H+L) Cross-Adsorbed Secondary Antibody, Alexa Fluor 488 (A-11008), was purchased from Thermo Fisher (IF); Goat anti-Mouse IgG (H+L) Cross-Adsorbed Secondary Antibody, Alexa Fluor 555 (A-21422), was purchased from Thermo Fisher (IF); Rabbit Polyclonal anti-SOX9 Antibody (PA5-81966) was purchased from Thermo Fisher (Wb); Rabbit Polyclonal anti- β -tubulin (44-344) was purchased from Thermo Fisher (IF, IHC); Mouse Monoclonal anti-Phospho-Tau antibody (clone: AT8; MN1020) was purchased from Thermo Fisher (IF, IHC); Rabbit Polyclonal anti-osteopontin antibody (PA5-34579) was purchased from Thermo Fisher (IF); Mouse Monoclonal anti-GAPDH antibody (clone: 6C5; AM4300) was purchased from Thermo Fisher (IF, Wb); Rabbit Polyclonal anti-RunX2 antibody (PA5-82787) was purchased from Thermo Fisher (Wb); Rabbit Polyclonal anti-NeuN antibody (PA5-78499) was purchased from Thermo Fisher (Wb); Mouse Monoclonal anti-BrdU antibody (clone: ZBU30; 03-3900) was purchased from Thermo Fisher (IF); Rabbit Polyclonal anti-Doublecortin antibody (48-1200) was purchased from Thermo Fisher (IF); Rabbit Polyclonal anti-alpha Actinin 1 Antibody (PA5-17308) was purchased from Thermo Fisher (IF, Wb); Goat anti-Mouse IgG (H+L) Secondary Antibody, HRP (31430) was purchased from Thermo Fisher (Wb, IHC); Goat anti-Rabbit IgG (H+L) Secondary Antibody, HRP (31460) was purchased from Thermo Fisher (Wb, IHC); Mouse Monoclonal anti-beta Tubulin (clone: AA10; 480011) was purchased from Thermo Fisher (IF); Rabbit Polyclonal anti-YAP1 Antibody (PA1-46189) was purchased from Thermo Fisher (IF)

Mouse monoclonal anti-Map2 antibody (clone: AP18; MA5-12826) was purchased from Thermo Fisher (IF, Flow); Rabbit polyclonal anti-GFAP antibody (PA5-16291) was purchased from Thermo Fisher (IF, Flow); Goat anti-Rabbit IgG (H+L) Cross-Adsorbed Secondary Antibody, Alexa Fluor 488 (A-11008), was purchased from Thermo Fisher (IF); Goat anti-Mouse IgG (H+L) Cross-Adsorbed Secondary Antibody, Alexa Fluor 555 (A-21422), was purchased from Thermo Fisher (IF); Rabbit Polyclonal anti-SOX9 Antibody (PA5-81966) was purchased from Thermo Fisher (Wb); Rabbit Polyclonal anti- β -tubulin (44-344) was purchased from Thermo Fisher (IF, IHC); Mouse Monoclonal anti-Phospho-Tau antibody (clone: AT8; MN1020) was purchased from Thermo Fisher (IF, IHC); Rabbit Polyclonal anti-osteopontin antibody (PA5-34579) was purchased from Thermo Fisher (IF); Mouse Monoclonal anti-GAPDH antibody

(clone:6C5; AM4300) was purchased from Thermo Fisher (IF, Wb); Rabbit Polyclonal anti-RunX2 antibody (PA5-82787) was purchased from Thermo Fisher (Wb); Rabbit Polyclonal anti-NeuN antibody (PA5-78499) was purchased from Thermo Fisher (Wb); Mouse Monoclonal anti-BrdU antibody (clone: ZBU30; 03-3900) was purchased from Thermo Fisher (IF); Rabbit Polyclonal anti-Doublecortin antibody (48-1200) was purchased from Thermo Fisher (IF); Rabbit Polyclonal anti-alpha Actinin 1 Antibody (PA5-17308) was purchased from Thermo Fisher (IF, Wb) ; Goat anti-Mouse IgG (H+L) Secondary Antibody, HRP (31430) was purchased from Thermo Fisher (Wb, IHC); Goat anti-Rabbit IgG (H+L) Secondary Antibody, HRP (31460) was purchased from Thermo Fisher (Wb, IHC). Mouse Monoclonal anti-beta Tubulin (clone: AA10; 480011) was purchased from Thermo Fisher (IF); Rabbit Polyclonal anti-YAP1 Antibody (PA1-46189) was purchased from Thermo Fisher (IF).

Validation

All antibodies are from commercially available sources and have been validated by the manufacturer. Supporting publications can be found on the manufacturer's website. See below for summary:

anti-Map2 antibody (Species: Avian, Bovine, Human, Mouse, Rat, Xenopus; Application: ICC, IF, IHC, Wb, Flow)
 anti-GFAP antibody (Species: Mouse, Non-human primate, Sheep, Rat, Bovine, Chicken, Guinea pig, Hamster, Human; Application: ICC, IF, Wb, IHC)
 Goat anti-Rabbit IgG (H+L) Cross-Adsorbed Secondary Antibody, Alexa Fluor 488 (Species: Rabbit; Application: Flow, ICC, IF, IHC, Wb)
 Goat anti-Mouse IgG (H+L) Cross-Adsorbed Secondary Antibody, Alexa Fluor 555 (Species: mouse; Application: Flow, ICC, IF, IHC, Wb)
 anti-SOX9 antibody (Species: Human, Mouse, Rat; Application: ICC, IF, IHC, Wb)
 anti-A β (1–42) antibody (Species: Human, Mouse, Non-human primate; Application: ELISA, ICC, IF, IHC, Wb)
 anti-Phospho-Tau antibody (Species: Artificial Control, Chicken, Dog, Fruit fly, Hamster, Human, Mouse, Non-human primate, Rabbit, Rat; Application: Flow, ICC, IF, IHC, Wb, ELISA)
 anti-osteopontin antibody (Species: Human, Mouse, Rat; Application: ICC, IF, IHC, Wb)
 anti-GAPDH antibody (Species: Amphibian, Dog, Chicken, Fish, Human, Mouse, Non-human primate, Rabbit, Rat; Application: IP, ICC, IF, DB, Wb)
 anti-RunX2 antibody (Species: Human; Application: ICC, IF, IHC, Wb)
 anti-NeuN antibody (Species: Human, Mouse, Rat; Application: ICC, IF, IHC, Wb)
 anti-BrdU antibody (Species: Chemical, Chicken, Mouse, Rabbit, Rat; Application: Flow, ICC, IF, IHC, IP)
 anti-Doublecortin antibody (Species: Human, Mouse, Rat; Application: ICC, IF, IP, Wb)
 anti-alpha Actinin 1 antibody (Species: Hamster, Human, Mouse, Non-human primate, Rat; Application: ICC, IF, Wb)
 Goat anti-Mouse IgG (H+L) Secondary Antibody, HRP (Species: mouse; Application: ELISA, ICC, IP, IHC, Wb)
 Goat anti-Rabbit IgG (H+L) Secondary Antibody, HRP (Species: Rabbit; Application: ELISA, IP, IHC, Wb)
 anti-beta Tubulin antibody (Species: Bovine, Human, Mouse, Rat; Application: ICC, IF, IHC, Wb)
 anti-YAP1 antibody (Species: Human, Mouse; Application: ICC, IF, IHC, Wb, ChIP)

Eukaryotic cell lines

Policy information about [cell lines](#)

Cell line source(s)

The neural stem cell line (OriCellTM C57BL/6) and the human bone-marrow mesenchymal stem cells were purchased from cyagen Biological Technology Co., Ltd, Suzhou, China.

Authentication

No cell-line authentication was performed.

Mycoplasma contamination

No testing for mycoplasma contamination was performed.

Commonly misidentified lines (See [ICLAC](#) register)

No commonly misidentified cell lines were used.

Animals and other organisms

Policy information about [studies involving animals](#); [ARRIVE guidelines](#) recommended for reporting animal research

Laboratory animals

Ten-month-old PrP-hApp/hPS1 double transgenic mice (2xTg-AD, PrP-hApp/hPS1 transgenic mice expressing a chimeric mouse/human amyloid precursor protein [APP] containing the Swedish K595N/M596L mutations and human PS1 with the deltaE9 mutation) were obtained from Zhishan Health Medical Research Institute (Beijing).

100 female C57BL/6 mice (12 weeks old) were obtained from Qinglong Mountain Animal Technology (Nanjing, China). After the study, the captive mice were killed via neck breaking (the most common method of killing mice with minimal pain, in line with animal welfare). The mice were stereotactically injected bilaterally with 5 μ L of NSCs at a rate of 0.3 μ L/min, and then brain tissue was collected, soaked in 10% formalin, and stored at 4°C for immunofluorescence and immunohistochemistry.

Wild animals

The study did not involve wild animals.

Field-collected samples

The study did not involve samples collected from the field.

Ethics oversight

All animal studies were performed according to institutional ethical guidelines, and were approved by the Committee on Animal Welfare of Jiangnan University.

Note that full information on the approval of the study protocol must also be provided in the manuscript.

Flow Cytometry

Plots

Confirm that:

- ☒ The axis labels state the marker and fluorochrome used (e.g. CD4-FITC).
- ☒ The axis scales are clearly visible. Include numbers along axes only for bottom left plot of group (a 'group' is an analysis of identical markers).
- ☒ All plots are contour plots with outliers or pseudocolor plots.
- ☒ A numerical value for number of cells or percentage (with statistics) is provided.

Methodology

Sample preparation

To determine the proportions of differentiated neurons and astrocytes under different culture conditions, the differentiated NSCs suspensions (1.0×10^6) were stained with a combination of antibodies: anti-Map2 monoclonal antibody and anti-GFAP polyclonal antibody. For the flow-cytometric analysis, the cells were fixed, permeabilized, blocked, and then incubated for 2 h with the primary antibodies diluted 1:500. Finally, the cells were incubated for 2 h with 1:200-diluted secondary antibodies (Alexa-Fluor®-488-conjugated goat anti-rabbit IgG [H+L] and Alexa-Fluor™-Plus-555-conjugated goat anti-mouse IgG [H+L]).

Instrument

BD FACSAria

Software

Data were analyzed with FlowJo.

Cell population abundance

Provided in Supplementary Fig. 11.

Gating strategy

No gating strategy was used.

☐ Tick this box to confirm that a figure exemplifying the gating strategy is provided in the Supplementary Information.